RESEARCH ARTICLE | MARCH 14 2024

Enhancement of localized superconductivity in $BaFe_2As_2$ films via Co-ion implantation

Myeongjun Oh ; Jongmin Lee ; Woun Kang ; Sanghan Lee ; Younjung Jo

APL Mater. 12, 031120 (2024)
https://doi.org/10.1063/5.0190904

Enhancement of localized superconductivity in $BaFe_2As_2$ films via Co-ion implantation

Cite as: APL Mater. 12, 031120 (2024); doi: 10.1063/5.0190904
Submitted: 9 December 2023 • Accepted: 26 February 2024 •
Published Online: 14 March 2024

Myeongjun Oh,[1] Jongmin Lee,[2,a)] Woun Kang,[3] Sanghan Lee,[2,b)] and Younjung Jo[1,b)]

AFFILIATIONS

[1] Deparment of Physics, Kyungpook National University, Daegu, South Korea
[2] School of Materials Science and Engineering, Gwangju Institute of Science and Technology, Gwangju, South Korea
[3] Department of Physics, Ewha Womans University, Seoul, South Korea

[a)] **Current address:** Department of Materials Science & Engineering and Materials Research Laboratory, University of Illinois at Urbana-Champaign, Urbana, IL 61801, USA.
[b)] **Authors to whom correspondence should be addressed:** sanghan@gist.ac.kr and jophy@knu.ac.kr

ABSTRACT

In this study, we present a novel approach to localized superconductivity induction in $BaFe_2As_2$ films via targeted implantation of cobalt (Co) ions. Primarily, our study focuses on the systematic distribution of Co ions and the subsequent evolution of superconducting properties in Co-ion-implanted $BaFe_2As_2$ films. Our observations show that Co-ion distribution in the films is congruent with the results of analytical methodologies employed in the semiconductor industry, as confirmed via transmission electron microscopy imaging. The temperature-dependent resistivity curves reveal the concurrent presence of superconducting and non-superconducting regions. Moreover, the superconducting domain demonstrates the typical diamagnetic behavior intrinsic in superconductors. Importantly, Co-ion concentrations of $\sim 10^{20}$ cm^{-3} can be achieved by finely tuning the beam energy and ion dose. This concentration is instrumental in establishing an effective superconducting percolation pathway within the films.

I. INTRODUCTION

Superconducting films have long been at the forefront of materials research as their importance has been supported by fundamental research dating back to the 1950s. The versatility of these thin films in a variety of applications has led to advances in fabrication technologies based on their unique characteristics. Traditionally, *in situ* fabrication techniques, such as pulsed laser deposition (PLD), sputtering, and chemical vapor deposition, have been primarily used in the field.[1–4] For films with intricate preparation requirements, *ex situ* methods, involving doping after the deposition of the precursor film, have been employed. A prevalent constraint with both techniques is the uniform doping across the entire film. While this uniform doping approach is effective for certain applications,[5,6] it falls short when localized doping is crucial for specific device architectures.[7,8] As the demand for precision and tailored applications grows, refined control methods are imperative for realizing the potential of superconducting films. Ion implantation, a prevalent technique in semiconductor device fabrication, enables targeted doping of intrinsic Si wafers for specific manufacturing purposes. A prominent advantage of this method is its precision; modulating the energy and dose of the ion beam affords granular control over both the doping region and intensity. In the established semiconductor realm, ion implantation has been instrumental in crafting intricate structures, including MOSFETs and CMOS devices.[9–13] Similarly, the superconducting domain boasts intricate devices, such as Superconducting QUantum Interference Device (SQUID) arrays, superconducting single-photon detectors (SSPD), and superconducting transistors and qubits.[14–17] Mass-production of these devices could draw from semiconductor fabrication techniques. Moreover, ion implantation plays a crucial role in probing the fundamental properties of superconductors, especially at their metal interfaces and grain boundaries.[18–22]

Ion implantation (irradiation) has been traditionally employed to enhance the superconducting properties of materials by establishing vortex pinning centers. This approach has been extended to diverse materials, including $YBa_2Cu_3O_{7-\delta}$ thin films,[23,24] $BaFe_2As_2$ single crystals family,[25] and Fe(Se, Te) thin films.[26] Indeed, there

is a notable study on inducing superconductivity through ion implantation into $SrFe_2As_2$ single crystals.[27] In our research, we have advanced the application of the ion implantation method in the field of superconductivity by employing it on thin films. This extension of the technique from single crystals to films opens up new avenues for exploring and manipulating superconducting properties in different material forms. Based on these investigations, we have distinguished potential applications of superconducting devices fabricated via this technique. Implementing ion implantation within the superconducting domain can pave the way for large-scale production of superconducting devices. In particular, superconductors in a layered $BaFe_2As_2$ can be fabricated using hole doping via Ba substitution, electron doping via Fe substitution, nonelectrical doping as seen with P doping, and by tailoring a Ba-122/$SrTiO_3$ superlattice with $SrTiO_3$.[28–31] This versatility expands potential applications.[32,33] However, the inherent anisotropy of superconductivity in high-temperature layered superconductors has limited its use in power transfer. The small electromagnetic anisotropy[34,35] found in $BaFe_2As_2$ makes it promising for superconducting devices.[36]

In this research, our primary objective was to develop a novel ion implantation method for producing $BaFe_2As_2$ superconducting films. This process transforms the treated region into a superconducting functional area, akin to doped semiconductors in conventional procedures. Our results highlight that the coexistence of a spin density wave (SDW) and superconducting states indicates the selective influence of irradiated dopant ions. Experiments revealed the optimal conditions for $BaFe_2As_2$ superconducting films using a Co-ion beam dose of ~10^{14} cm^{-2} at under 80 keV. Our study emphasizes that higher ion concentrations can be achieved via ideally doped phases by modulating the irradiation energy, provided the inflicted damage is minimal.

II. METHODS

We deposited the $BaFe_2As_2$ precursor film on a CaF_2 substrate using PLD and achieved doping via Co-ion implantation. The ion implantation was performed at the Korea Multi-purpose Accelerator Complex (KOMAC). A schematic representation of the film is shown in Fig. 1(a). The films were sufficiently thick (460 nm) to encompass the Co-ion distribution profile, positioning Co ions near the surface of the $BaFe_2As_2$ film. The pristine $BaFe_2As_2$ films were irradiated with a Co-ion beam characterized by an energy range of 20–100 keV, a dose spanning from 5×10^{12} to 1×10^{16} cm^{-2}, and an incident angle perpendicular to the film surface. The depth profile of implanted Co ions was analyzed by utilizing time-of-flight secondary-ion mass spectrometry (TOF-SIMS). The sample was cooled in a closed-cycle refrigerator to assess the superconducting phase of the film, and transport measurements were performed using the four-terminal method. Susceptibility was measured along the in-plane using a superconducting quantum interference device magnetometer (Magnetic Property Measurement System, Quantum Design).

III. RESULTS AND DISCUSSION

A. Ion distribution analysis

We focused on the ion distribution and on the influence of ion implantation on it. Figure 1(b) shows the TOF-SIMS elemental

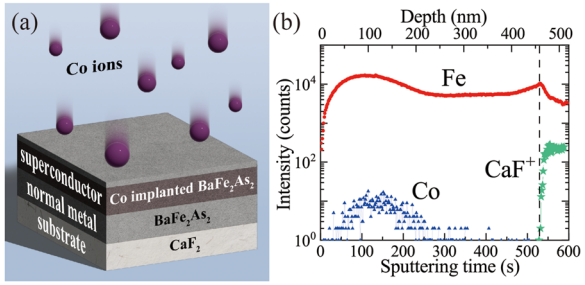

FIG. 1. (a) Schematics of the Co-ion implantation process in $BaFe_2As_2$ films. (b) Time-of-flight secondary ion mass spectrometry (TOF-SIMS) profile over time. The time axis is converted to depth by considering the distribution of constituents within the film and the substrate.

depth profiles of the film, which was implanted using a Co beam with a beam dose of 1×10^{14} cm^{-2} and an energy value of 80 keV. The horizontal axis represents the time of sputtering with oxygen ions from the film surface. Our pristine $BaFe_2As_2$ films showed a homogeneous structure,[37] resulting in a consistent sputtering rate. As such, the sputtering time can be directly correlated with the depth of the film. The CaF^+ ion signal corresponding to the substrate composition first emerged at 528 s (dashed line), suggesting that the entire pristine $BaFe_2As_2$ film was peeled off by this time. By converting 528 s to the thickness observed in the secondary electron microscopy (SEM) image (460 nm), we deduced the sputtering time-to-depth conversion ratio. We plotted three curves for CaF^+ (green), Fe (red), and Co (blue) to distinguish the depth distribution of Co ions. The increase in the Fe ion concentration near the surface coincided with the distribution of Co ions, indicating collisions between the incoming Co ions and the lattice Fe ions.[38] CaF^+ was observed at the second peaks of the Fe ion profiles.

Top of Fig. 2(a) shows the depth profiles of $BaFe_2As_2$ films with Co-ion implantation at a dose of 10^{14} cm^{-2} at various energies. A consistent shift was observed in Co-ion distribution with the irradiation energy, resembling a Gaussian distribution (marked by the red dashed line). Greater ion beam energies resulted in deeper and wider Co-ion distributions. Given that the total number of implanted ions

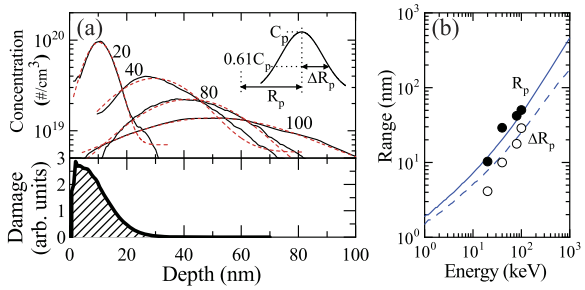

FIG. 2. (a) (Top) TOF-SIMS profiles of Co ions at varying energies (black solid lines) and their Gaussian fits (red dotted lines). (Inset) Displays the peak concentration, C_p, the depth, R_p, where the peak occurs, and the width, ΔR_p, at 61% of C_p. (Bottom) Depth-dependent damage at 20 keV, as predicted by the SRIM simulations. (b) The values of R_p and ΔR_p as functions of the Co-ion energy and those obtained from the simulations (blue lines).

remained unchanged, the peak height decreased as the distribution widened. This pattern is typical in ion implantation processes.[37] Energetic ions penetrating the substrate interact with atoms in the film, losing energy. This interaction statistically fluctuates; consequently, ions move zig-zag owing to multiple scatterings from target atoms. The inset of Fig. 2(a) shows that C_p is the doping level, R_p is the doping depth, and ΔR_p is the doping width represented by the half-width at $0.61 \times C_p$. Using the Gaussian approximation, the ion concentration based on the range, $C(x)$, is given by[39]

$$C(x) = \frac{\Phi}{\sqrt{2\pi}\Delta R_p} \exp\left(-\frac{(x - R_p)^2}{2\Delta R_p^2}\right), \quad (1)$$

where Φ is the dose of the Co-ion beam, R_p is the mode, and ΔR_p is the longitudinal straggle. The projected range, R_p, indicates the average penetration depth from the target surface to its peak. The range straggle, the deviation in the ion's travel distance from the target's surface to its final depth, arises owing to the energy straggle.

To determine the acceleration energy for a designated doping depth, we compared the TOF-SIMS results to the outcomes from the stopping and range of ions in matter (SRIM) and transport of ions in matter (TRIM) simulators, common tools in semiconductor research.[40–42] A Ba:Fe:As stoichiometric ratio of 1:2:2 and a density of 6.64 g/cm^3 were used as input parameters for the simulations.[43] Figure 2(b) shows R_p (closed symbols) and ΔR_p (open symbols) values for various energies. We found that R_p and ΔR_p values from the simulations (plotted as blue lines) matched well with the experimental findings. Furthermore, at the bottom of Fig. 2(a), we incorporated the depth curve from the TRIM simulator to evaluate the potential sample damage due to vacancy creation. Notably, while ion implantation typically induces vacancies near the surface, they are rarely found beyond 40 nm from the surface. This suggests that a 20 keV ion beam exposure degrades the crystalline structure of the $BaFe_2As_2$ film up to a thickness of 40 nm.

Figures 3(a) and 3(b) show the cross-sectional transmission electron microscope (TEM) images of the film before and after Co-ion implantation with an energy of 20 keV and a beam dose of 5×10^{15} cm^{-2}, respectively. We fabricated a 650 nm thick pure $BaFe_2As_2$ film to account for the ~200 nm reaction layer forming at the interface of the $BaFe_2As_2$ film and the CaF_2 substrate. This ensures that superconducting properties manifest in regions far from the reaction layer. We observed a superficial 20 nm amorphized layer on top of the pristine film [Fig. 3(a)], potentially preventing the ion-tunneling effect that otherwise expends the distribution tail of the implanted ion. This amorphous layer originates from vacancies formed upon the reaction of Ba ions and hydration.[44] After implantation, Fig. 3(b) shows a substantial and uniform amorphous layer on the surface of the film. In addition, the amorphous or crystalline state of each region was verified through fast Fourier transform (FFT) analysis.[45,46] Assuming that the doped regions turned into superconductors and the implanted regions became amorphous, the superconducting phase spanned the film evenly. The ion implantation-induced amorphous layer had a thickness of around 39 nm, consistent with the TRIM-simulated damage region thickness.

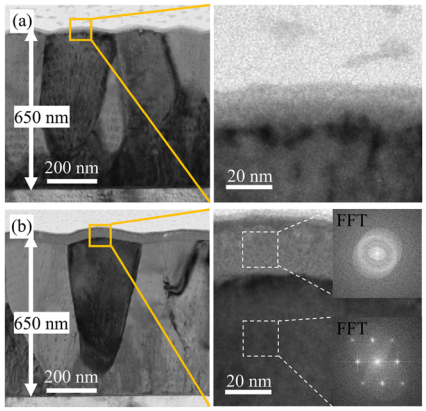

FIG. 3. Cross-sectional transmission electron microscopy (TEM) images of (a) a pristine $BaFe_2As_2$ film and (b) a Co-ion implanted $BaFe_2As_2$ film. The pristine film exhibits a thin amorphous layer atop, attributed to the inherent volatility of As ions. The Co-ion-implanted $BaFe_2As_2$ film displays an amorphous layer whose thickness aligns with the predictions from Fig. 2(a). Fast Fourier transform (FFT) images for each corresponding region clearly distinguishes between their amorphous and crystalline characteristics.

B. Superconductivity analysis

We anticipate the formation of a heterostructure, in which the implanted region near the surface manifests as the electron-doped phase, while the deeper portion remains the underdoped phase. In Fig. 4(a), the temperature-dependent resistivity, $\rho(T)$, of the implanted films is plotted down to 4 K (black line), with a beam dose set at 10^{14} cm^{-2} and the energy at 20 keV. The solid and dashed green lines represent the resistivity curves for pure $BaFe_2As_2$ and its optimally Co-doped $BaFe_2As_2$, respectively. The pure $BaFe_2As_2$ shows an SDW transition near 140 K,[47] whereas optimally Co-doped $BaFe_2As_2$ shows a superconducting transition at 23 K.[48,49] Notably, the pure and optimally doped $BaFe_2As_2$ phases seemed to coexist independently within the film. This dual transition presence indicates that the influence of irradiated dopant ions is depth-specific rather than comprehensively affecting the entire film area, as illustrated in Fig. 1. The magnetic property measurements further confirmed superconductivity. Figure 4(b) shows that

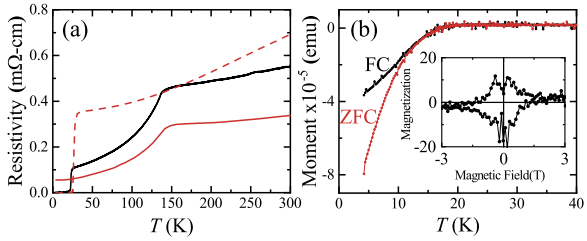

FIG. 4. Superconducting properties of Co-ion-implanted films. (a) Temperature-dependent transport behavior of the films (black line). The solid and dotted green lines correspond to the pristine and optimally Co-doped $BaFe_2As_2$, respectively. (b) The magnetic behavior under an externally applied perpendicular magnetic field is characterized through field cooling and zero-field cooling methods. The inset displays the magnetic hysteresis observed in the films.

when a 10 Oe magnetic field is applied perpendicular to the surface, the material exhibits superconducting diamagnetism, which becomes apparent below 20 K. As the temperature decreases, the extent of the superconducting volume within the material increases. The variation in the critical temperature (T_c) compared to the resistivity is attributed to the coexistence of diverse doping levels. In the inset of Fig. 4(b), the magnetization at 5 K shows a diamond-shaped curve typical for superconductivity, signifying a creation of a superconducting percolation pathway.

Figure 5 shows the temperature-dependent resistivity, $\rho(T)$, of the film under various conditions. The left column [Figs. 5(a)–5(c)] presents variations based on the beam dose, while the right column [Figs. 5(d)–5(f)] presents variations resulting from changes in the beam energy. Figure 5(a) shows the $\rho(T)$ curve for the film implanted with various beam doses and a fixed beam energy of 20 keV. A subtle kink around 10 K in the undoped as-grown film indicates the emergence of superconductivity owing to strain effects between the substrate and the material. For a dose of 5×10^{12} cm^{-2}, the temperature of kink increased, but the decrease in resistivity was very broad. At 5×10^{13} cm^{-2}, the superconducting transition was sharp, and the T_c value was high, but the residual resistivity appeared at low temperatures. The optimal superconducting transition occurred at a dose of 1×10^{14} cm^{-2}. Beyond this optimal dose, the superconducting phase began to diminish.

We evaluated $\rho(T)$ on two criteria. First, we normalized ρ(4 K) to ρ(300 K) to compare the quality of superconductivity. As shown in Fig. 5(b), the normalized resistivity consistently decreased with increasing beam dose, reaching zero at a beam dose of 10^{14} cm^{-2}. However, at higher doses, the residual resistance increased. Second, we compared the critical temperature T_c^{mid} (symbols) and ΔT_c (error bars), as shown in Fig. 5(c). Typically, T_c^{onset}, the temperature at which resistance starts to decrease, serves as a point of comparison. In our films, this value remained relatively consistent (shaded region), suggesting the occurrence of filamentary superconductivity.[50] This T_c^{onset} is analogous to T_c at the optimal doping level. Here, ΔT_c is determined based on the difference between T_c^{onset} and T_c^{offset} (the temperature where the resistance becomes zero). Several samples showed residual resistance, resulting in a pronounced ΔT_c. The best superconducting quality was identified at a beam dose of 10^{14} cm^{-2}, with T_c^{mid} at the maximum and ΔT_c at the minimum. For a beam dose below 10^{14} cm^{-2}, an inadequate number of dopant ions prevented the establishment of sufficient superconducting percolation pathways. Conversely, doses above this threshold led to significant amorphization due to ion disorder in the lattice.

Figure 5(d) shows the superconducting transitions in the implanted films at energies of 20, 40, 80, and 100 keV for a beam dose of 10^{14} cm^{-2}. The residual resistance was negligible for beam energies below 80 keV, whereas at 100 keV, a finite resistance emerged [Fig. 5(e)]. As shown in Fig. 5(f), as the beam energy decreased, T_c^{mid} increased and ΔT_c decreased. This is due to the increase in ion concentration with a decrease in the energy, indicating that optimal percolation paths are achievable only within specific energy levels. A small value of ΔT_c at low energy indicates the ideal ion concentration for producing the Co-doped $BaFe_2As_2$ superconducting phase. In fact, controlling Co doping depth becomes feasible with beam energies below 80 keV.

The consolidated findings reveal the critical concentration governing the superconducting percolation path. In [Eq. (1)], we primarily focus on the peak concentration C_p at R_p, and to ascertain the C_p, we referred to the experimental beam doses and corresponding ΔR_p values shown in Fig. 2(b). Figure 6 shows the interplay between T_c^{mid} and C_p. The red and black curves denote the

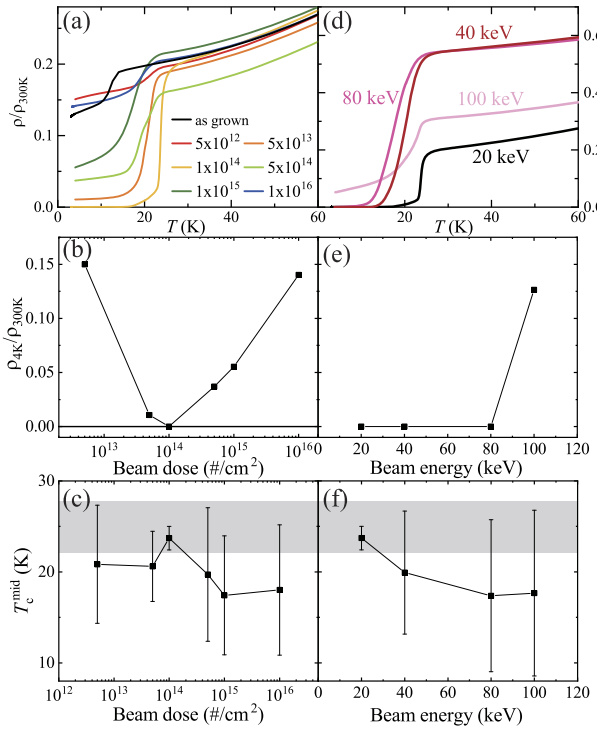

FIG. 5. Comprehensive study of resistivity and critical temperatures. (a) Temperature-dependent resistivity, normalized by its value at 300 K, for different beam doses. (b) Resistivity at 4 K normalized by its value at 300 K. At a beam dose of 10^{14}, the curve attains a minimum, with its value approaching zero. (c) Critical temperature, T_c^{mid}, plotted as a function of beam dose, with ΔT_c indicated by the error bars. (d) Resistivity normalized by its value at 300 K for different beam energies. (e) Resistivity at 4 K normalized by its value at 300 K. (f) T_c^{mid} plotted as a function of beam energy, with ΔT_c represented by the error bars.

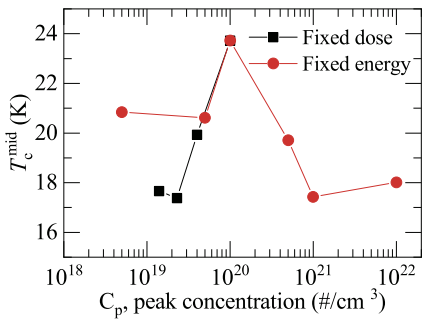

FIG. 6. T_c^{mid} in relation to C_p: Based on Figs. 5(c) and 5(f), using beam dose and beam energy as parameters, peak concentrations are calculated. T_c^{mid} reaches its maximum at a C_p value of approximately 10^{20}.

T_c^{mid} values under constant energy and beam dose, respectively. For both curves, T_c^{mid} peaked at a concentration of 10^{20} cm^{-3}, and this concentration can be converted to 0.5% of Fe ions. This level belongs to the filamentary superconductivity, and when subjected to a dose ten times higher, the phase diagram suggests the emergence of a superconducting phase. However, due to the amorphization, this transition does not occur as anticipated. Despite a consistent C_p value, depth profiles can vary based on implantation conditions. Increasing the irradiation energy broadens the ion distribution. In contrast, modifying the irradiation dose does not affect the shape of the distribution. Consequently, by adjusting the irradiation parameters in both the dose and energy, we can potentially govern the uniformity of the ion distribution, providing a mechanism to modulate the T_c value.

IV. CONCLUSIONS

In this study, we investigated the formation of the superconducting phase in $BaFe_2As_2$ films using localized Co-ion implantation—a technique commonly employed in the integrated circuit industry. Using a Gaussian function, we accurately modeled the depth profile of Co ions, enabling an enhanced and better understanding of ion-doped superconductors through the SRIM simulator.

Our results delineate the critical balance between ion doses and beam energies that either promote or inhibit the formation of superconducting percolation paths. An insufficiently low dose may fail to introduce a sufficient amount of the superconducting phase to establish a percolation trajectory. Conversely, an exceedingly high dose or energy might detrimentally impact the film. The optimal ion beam conditions produce Co-ion concentrations of ~10^{20} cm^{-3}, favoring the formation of superconducting percolation paths in the film. This study deepens our comprehension of how ion implantation influences superconductivity in iron-based compounds, especially $BaFe_2As_2$. Our insights pave the way for tailoring their superconducting properties for diverse applications ranging from energy transmission to advanced medical technologies.

ACKNOWLEDGMENTS

Y.J. acknowledges the funding by the National Research Foundation of Korea (NRF) [Grant Nos. 2019R1A2C1089017, 2022H1D3A3A01077468 (BrainLink Program), and RS-2023-00301914 (LAMP Program)]. A portion of this work was performed at the Korean Basic Science Institute (KBSI) and Korea Multi-purpose Accelerator Complex (KOMAC). W.K. was supported by the National Research Foundation of Korea (NRF) under Grant Nos. 2018R1D1A1B07050087 and 2018R1A6A1A03025340. A portion of this work was performed at the National High Magnetic Field Laboratory, which is supported by National Science Foundation Cooperative Agreement No. DMR-2128556 and the State of Florida.

AUTHOR DECLARATIONS

Conflict of Interest

The authors have no conflicts to disclose.

Author Contributions

Myeongjun Oh: Conceptualization (equal); Formal analysis (equal); Investigation (lead); Methodology (lead); Writing – original draft (lead); Writing – review & editing (lead). **Jongmin Lee**: Conceptualization (equal); Methodology (equal); Writing – review & editing (equal). **Woun Kang**: Conceptualization (equal); Formal analysis (equal); Investigation (lead); Methodology (equal); Writing – original draft (lead). **Sanghan Lee**: Conceptualization (equal); Methodology (equal); Writing – review & editing (equal). **Younjung Jo**: Conceptualization (lead); Methodology (equal); Writing – original draft (lead); Writing – review & editing (lead).

DATA AVAILABILITY

The data that support the findings of this study are available within the article.

REFERENCES

[1] S. Lee, J. Jiang, Y. Zhang, C. Bark, J. Weiss, C. Tarantini, C. Nelson, H. Jang, C. Folkman, S. Baek *et al.*, "Template engineering of Co-doped $BaFe_2As_2$ single-crystal thin films," Nat. Mater. **9**, 397–402 (2010).
[2] A. Brinkman, D. Mijatovic, G. Rijnders, V. Leca, H. Smilde, I. Oomen, A. A. Golubov, F. Roesthuis, S. Harkema, H. Hilgenkamp *et al.*, "Superconducting thin films of MgB_2 on Si by pulsed laser deposition," Physica C **353**, 1–4 (2001).
[3] S. Speller, C. Aksoy, M. Saydam, H. Taylor, G. Burnell, A. Boothroyd, and C. Grovenor, "Analysis of $Fe_ySe_{1-x}Te_x$ thin films grown by radio frequency sputtering," Supercond. Sci. Technol. **24**, 075023 (2011).
[4] D. Hu, C. Ye, X. Wang, X. Zhao, L. Kang, J. Liu, R. Duan, X. Cao, Y. He, J. Hu *et al.*, "Chemical vapor deposition of superconducting $FeTe_{1-x}Se_x$ nanosheets," Nano Lett. **21**, 5338–5344 (2021).
[5] J. Smith, M. Cima, and N. Sonnenberg, "High critical current density thick MOD-derived YBCO films," IEEE Trans. Appl. Supercond. **9**, 1531–1534 (1999).
[6] E. Fortunato, P. Barquinha, and R. Martins, "Oxide semiconductor thin-film transistors: A review of recent advances," Adv. Mater. **24**, 2945–2986 (2012).
[7] Y. J. Chung, W. J. Choi, S. G. Kang, C. W. Lee, J.-O. Lee, K.-J. Kong, and Y. K. Lee, "A study on the influence of local doping in atomic layer deposited Al:ZnO thin film transistors," J. Mater. Chem. C **2**, 9274–9282 (2014).
[8] P. Livshits, V. Dikhtyar, A. Inberg, A. Shahadi, and E. Jerby, "Local doping of silicon by a point-contact microwave applicator," Microelectron. Eng. **88**, 2831–2836 (2011).
[9] C. Selvakumar and B. Hecht, "SiGe-channel n-MOSFET by germanium implantation," IEEE Electron Device Lett. **12**, 444–446 (1991).
[10] H. Kambayashi, Y. Niiyama, S. Ootomo, T. Nomura, M. Iwami, Y. Satoh, S. Kato, and S. Yoshida, "Normally off n-channel GaN MOSFETs on Si substrates using an SAG technique and ion implantation," IEEE Electron Device Lett. **28**, 1077–1079 (2007).
[11] K. Izumi, M. Doken, and H. Ariyoshi, "CMOS devices fabricated on buried SiO_2 layers formed by oxygen implantation into silicon," Electron. Lett. **14**, 593 (1978).
[12] T. Ohzone, H. Shimura, K. Tsuji, and T. Hirao, "Silicon-gate n-well CMOS process by full ion-implantation technology," IEEE Trans. Electron Devices **27**, 1789–1795 (1980).
[13] A. Stolmeijer, "A twin-well CMOS process employing high-energy ion implantation," IEEE Trans. Electron Devices **33**, 450–457 (1986).
[14] G. V. Prokopenko, O. A. Mukhanov, A. Leese de Escobar, B. Taylor, M. De Andrade, S. Berggren, P. Longhini, A. Palacios, M. Nisenoff, and R. L. Fagaly, "DC and RF measurements of serial bi-SQUID arrays," IEEE Trans. Appl. Supercond. **23**, 1400607 (2012).
[15] G. Gol'tsman, O. Okunev, G. Chulkova, A. Lipatov, A. Semenov, K. Smirnov, B. Voronov, A. Dzardanov, C. Williams, and R. Sobolewski, "Picosecond superconducting single-photon optical detector," Appl. Phys. Lett. **79**, 705–707 (2001).

[16]A. N. McCaughan and K. K. Berggren, "A superconducting-nanowire three-terminal electrothermal device," Nano Lett. **14**, 5748–5753 (2014).
[17]A. Wallraff, D. I. Schuster, A. Blais, L. Frunzio, R.-S. Huang, J. Majer, S. Kumar, S. M. Girvin, and R. J. Schoelkopf, "Strong coupling of a single photon to a superconducting qubit using circuit quantum electrodynamics," Nature **431**, 162–167 (2004).
[18]N. Reyren, S. Thiel, A. Caviglia, L. F. Kourkoutis, G. Hammerl, C. Richter, C. W. Schneider, T. Kopp, A. S. Rüetschi, D. Jaccard *et al.*, "Superconducting interfaces between insulating oxides," Science **317**, 1196–1199 (2007).
[19]G. Zerweck, "On pinning of superconducting flux lines by grain boundaries," J. Low Temp. Phys. **42**, 1–9 (1981).
[20]J. Linder and J. W. Robinson, "Superconducting spintronics," Nat. Phys. **11**, 307–315 (2015).
[21]P. Van Son, H. Van Kempen, and P. Wyder, "New method to study the proximity effect at the normal-metal–superconductor interface," Phys. Rev. Lett. **59**, 2226 (1987).
[22]J. Chakhalian, J. Freeland, G. Srajer, J. Strempfer, G. Khaliullin, J. Cezar, T. Charlton, R. Dalgliesh, C. Bernhard, G. Cristiani *et al.*, "Magnetism at the interface between ferromagnetic and superconducting oxides," Nat. Phys. **2**, 244–248 (2006).
[23]B. Aichner, B. Müller, M. Karrer, V. R. Misko, F. Limberger, K. L. Mletschnig, M. Dosmailov, J. D. Pedarnig, F. Nori, R. Kleiner *et al.*, "Ultradense tailored vortex pinning arrays in superconducting $YBa_2Cu_3O_{7-\delta}$ thin films created by focused He ion beam irradiation for fluxonics applications," ACS Appl. Nano Mater. **2**, 5108–5115 (2019).
[24]H. Matsui, T. Ootsuka, H. Ogiso, H. Yamasaki, M. Sohma, I. Yamaguchi, T. Kumagai, and T. Manabe, "Enhancement of critical current density in $YBa_2Cu_3O_7$ films using a semiconductor ion implanter," J. Appl. Phys. **117**, 043911 (2015).
[25]D. Torsello, L. Gozzelino, R. Gerbaldo, T. Tamegai, and G. Ghigo, "Scaling laws for ion irradiation effects in iron-based superconductors," Sci. Rep. **11**, 5818 (2021).
[26]D. Torsello, M. Fracasso, R. Gerbaldo, G. Ghigo, F. Laviano, A. Napolitano, M. Iebole, M. Cialone, N. Manca, A. Martinelli *et al.*, "Proton irradiation effects on the superconducting properties of Fe(Se,Te) thin films," IEEE Trans. Appl. Supercond. **32**, 7500105 (2022).
[27]S. Chong, J. Tallon, F. Fang, J. Kennedy, K. Kadowaki, and G. Williams, "Surface superconductivity on $SrFe_2As_2$ single crystals induced by ion implantation," Europhys. Lett. **94**, 37009 (2011).
[28]M. Rotter, M. Tegel, and D. Johrendt, "Superconductivity at 38 K in the iron arsenide $(Ba_{1-x}K_x)$ Fe_2As_2," Phys. Rev. Lett. **101**, 107006 (2008).
[29]L. Li, Y. Luo, Q. Wang, H. Chen, Z. Ren, Q. Tao, Y. Li, X. Lin, M. He, Z. Zhu *et al.*, "Superconductivity induced by Ni doping in $BaFe_2As_2$ single crystals," New J. Phys. **11**, 025008 (2009).
[30]K. Hashimoto, M. Yamashita, S. Kasahara, Y. Senshu, N. Nakata, S. Tonegawa, K. Ikada, A. Serafin, A. Carrington, T. Terashima *et al.*, "Line nodes in the energy gap of superconducting $BaFe_2(As_{1-x}P_x)_2$ single crystals as seen via penetration depth and thermal conductivity," Phys. Rev. B **81**, 220501 (2010).
[31]J.-H. Kang, J.-W. Kim, P. J. Ryan, L. Xie, L. Guo, C. Sundahl, J. Schad, N. Campbell, Y. G. Collantes, E. E. Hellstrom *et al.*, "Superconductivity in undoped $BaFe_2As_2$ by tetrahedral geometry design," Proc. Natl. Acad. Sci. U. S. A. **117**, 21170–21174 (2020).
[32]M. Noe and M. Steurer, "High-temperature superconductor fault current limiters: Concepts, applications, and development status," Supercond. Sci. Technol. **20**, R15 (2007).
[33]M. H. Devoret and R. J. Schoelkopf, "Superconducting circuits for quantum information: An outlook," Science **339**, 1169–1174 (2013).
[34]A. Yamamoto, J. Jaroszynski, C. Tarantini, L. Balicas, J. Jiang, A. Gurevich, D. Larbalestier, R. Jin, A. Sefat, M. A. McGuire *et al.*, "Small anisotropy, weak thermal fluctuations, and high field superconductivity in Co-doped iron pnictide $Ba(Fe_{1-x}Co_x)_2As_2$," Appl. Phys. Lett. **94**, 062511 (2009).
[35]Y. Jo, J. Jaroszynski, A. Yamamoto, A. Gurevich, S. Riggs, G. Boebinger, D. Larbalestier, H. Wen, N. Zhigadlo, S. Katrych *et al.*, "High-field phase-diagram of Fe arsenide superconductors," Physica C **469**, 566–574 (2009).
[36]M. Kano, Y. Kohama, D. Graf, F. Balakirev, A. S Sefat, M. A Mcguire, B. C Sales, D. Mandrus, and S. W Tozer, "Anisotropy of the upper critical field in a Co-doped $BaFe_2As_2$ single crystal," J. Phys. Soc. Jpn. **78**, 084719 (2009).
[37]S. Lee, C. Tarantini, P. Gao, J. Jiang, J. Weiss, F. Kametani, C. Folkman, Y. Zhang, X. Pan, E. Hellstrom *et al.*, "Artificially engineered superlattices of pnictide superconductors," Nat. Mater. **12**, 392–396 (2013).
[38]M. L. Roush, T. D. Andreadis, F. Davarya, and O. F. Goktepe, "Dynamic simulation of changes in near-surface composition during ion bombardment," Appl. Surf. Sci. **11-12**, 235–242 (1982).
[39]H. Oechsner, *Thin Film and Depth Profile Analysis*, 37 (Springer Science & Business Media, 2013).
[40]P. Li, S. Chen, H. Dai, Z. Yang, Z. Chen, Y. Wang, Y. Chen, W. Peng, W. Shan, and H. Duan, "Recent advances in focused ion beam nanofabrication for nanostructures and devices: Fundamentals and applications," Nanoscale **13**, 1529–1565 (2021).
[41]Q. Wang, Z. Yao, C. Zhao, T. Verhallen, D. P. Tabor, M. Liu, F. Ooms, F. Kang, A. Aspuru-Guzik, Y.-S. Hu *et al.*, "Interface chemistry of an amide electrolyte for highly reversible lithium metal batteries," Nat. Commun. **11**, 4188 (2020).
[42]R. Gong, G. He, X. Gao, P. Ju, Z. Liu, B. Ye, E. A. Henriksen, T. Li, and C. Zu, "Coherent dynamics of strongly interacting electronic spin defects in hexagonal boron nitride," Nat. Commun. **14**, 3299 (2023).
[43]M. Martin, "High-temperature superconductivity in doped $BaFe_2As_2$," Ph.D. thesis, LMU, 2011.
[44]T. Katase, H. Hiramatsu, H. Yanagi, T. Kamiya, M. Hirano, and H. Hosono, "Atomically-flat, chemically-stable, superconducting epitaxial thin film of iron-based superconductor, cobalt-doped $BaFe_2As_2$," Solid State Commun. **149**, 2121–2124 (2009).
[45]R. Matassa, S. Orlanducci, G. Reina, M. C. Cassani, D. Passeri, M. L. Terranova, and M. Rossi, "Structural and morphological peculiarities of hybrid Au/nanodiamond engineered nanostructures," Sci. Rep. **6**, 31163 (2016).
[46]S. Hong, C.-S. Lee, M.-H. Lee, Y. Lee, K. Y. Ma, G. Kim, S. I. Yoon, K. Ihm, K.-J. Kim, T. J. Shin *et al.*, "Ultralow-dielectric-constant amorphous boron nitride," Nature **582**, 511–514 (2020).
[47]M. Rotter, M. Tegel, D. Johrendt, I. Schellenberg, W. Hermes, and R. Pöttgen, "Spin-density-wave anomaly at 140 K in the ternary iron arsenide $BaFe_2As_2$," Phys. Rev. B **78**, 020503 (2008).
[48]N. Ni, M. Tillman, J.-Q. Yan, A. Kracher, S. Hannahs, S. L. Bud'ko, and P. Canfield, "Effects of Co substitution on thermodynamic and transport properties and anisotropic H_{c2} in $Ba(Fe_{1-x}Co_x)_2As_2$ single crystals," Phys. Rev. B **78**, 214515 (2008).
[49]A. Lucarelli, A. Dusza, F. Pfuner, P. Lerch, J. G. Analytis, J.-H. Chu, I. R. Fisher, and L. Degiorgi, "Charge dynamics of Co-doped $BaFe_2As_2$," New J. Phys. **12**, 073036 (2010).
[50]H. Xiao, T. Hu, S. He, B. Shen, W. Zhang, B. Xu, K. He, J. Han, Y. Singh, H. Wen *et al.*, "Filamentary superconductivity across the phase diagram of $Ba(Fe,Co)_2As_2$," Phys. Rev. B **86**, 064521 (2012).